

PAPER

Element-specific density profiles in interacting biomembrane models

To cite this article: Emanuel Schneck *et al* 2017 *J. Phys. D: Appl. Phys.* **50** 104001

View the [article online](#) for updates and enhancements.

You may also like

- [RGDK-lipopeptide for targeting genetic vaccines to antigen presenting cells](#)
Wahida Rahaman and Arabinda Chaudhuri
- [Combined effects of headgroup charge and tail unsaturation of lipids on lateral organization and diffusion of lipids in model biomembranes](#)
Xiao-Jie Chen, , Qing Liang et al.
- [Ripple Phase Behavior in Mixtures of DPPC/POPC lipids: SAXS and SANS Studies](#)
D V Soloviov, Yu E Gorshkova, O I Ivankov et al.



ECS
The
Electrochemical
Society
Advancing solid state &
electrochemical science & technology

DISCOVER
how sustainability
intersects with
electrochemistry & solid
state science research

Element-specific density profiles in interacting biomembrane models

Emanuel Schneck^{1,6}, Ignacio Rodriguez-Loureiro¹, Luca Bertinetti¹, Egor Marin², Dmitri Novikov³, Oleg Konovalov⁴ and Georgi Gochev^{1,5}

¹ Max Planck Institute of Colloids and Interfaces, Am Mühlenberg 1, 14476 Potsdam, Germany

² Moscow Institute of Physics and Technology (MIPT), 141700 Dolgoprudniy, Russia

³ Deutsches Elektronen-Synchrotron (DESY), 22607 Hamburg, Germany

⁴ ESRF, The European Synchrotron, 71 avenue des Martyrs, 38000 Grenoble, France

⁵ Institute of Physical Chemistry, Bulgarian Academy of Sciences, 1113 Sofia, Bulgaria

E-mail: schneck@mpikg.mpg.de

Received 8 September 2016, revised 23 December 2016

Accepted for publication 17 January 2017

Published 9 February 2017



Abstract

Surface interactions involving biomembranes, such as cell–cell interactions or membrane contacts inside cells play important roles in numerous biological processes. Structural insight into the interacting surfaces is a prerequisite to understand the interaction characteristics as well as the underlying physical mechanisms. Here, we work with simplified planar experimental models of membrane surfaces, composed of lipids and lipopolymers. Their interaction is quantified in terms of pressure–distance curves using ellipsometry at controlled dehydrating (interaction) pressures. For selected pressures, their internal structure is investigated by standing-wave x-ray fluorescence (SWXF). This technique yields specific density profiles of the chemical elements P and S belonging to lipid headgroups and polymer chains, as well as counter-ion profiles for charged surfaces.

Keywords: surfaces, interfaces, lipid membranes, x-ray scattering, polymer brushes

 Supplementary material for this article is available [online](#)

(Some figures may appear in colour only in the online journal)

1. Introduction

Nanometric layers formed by molecular assemblies in 2D architectures are major components of soft and biological matter [1, 2]. Their structural organization and biological or technological functions are highly sensitive to the mutual interactions of their surfaces in the aqueous environment [1, 3]. Important examples in biology are the membranes of cells and organelles, which are typically found under rather crowded conditions [4], so that membrane–membrane interactions play a key role for their functions. The character of the interaction in terms of magnitude and range, as well as whether it is mainly attractive or repulsive, affects cell

adhesion [5, 6], vesicle release, the spontaneous formation of membrane stacks [7] and the properties of bacterial biofilms [8]. It in general involves spatially extended (generic) and specific ligand-receptor contributions and is determined by the chemical composition of the membrane surfaces comprising neutral and charged lipid head groups and membrane-bound saccharides, polypeptides, and macromolecules. Similarly, the interaction between technological interfaces also plays an important role in a multitude of applications such as liquid purification and separation chemistry [9], or lubrication [10]. Liquid/liquid interfaces, for example, are commonly stabilized by self-assembled amphiphilic molecules including surfactants, proteins, and polymers, with the aim of rendering their mutual interaction predominantly repulsive thus providing stability of (‘soft’) colloids [11].

The interaction between two surfaces across water is typically described in terms of pressure–distance curves, which relate the interaction (or: disjoining) pressure Π to the

⁶ This article belongs to the [special issue: Emerging Leaders](#), which features invited work from the best early-career researchers working within the scope of *J. Phys. D*. This project is part of the *Journal of Physics* series’ 50th anniversary celebrations in 2017. Emanuel Schneck was selected by the Editorial Board of *J. Phys. D* as an emerging leader.

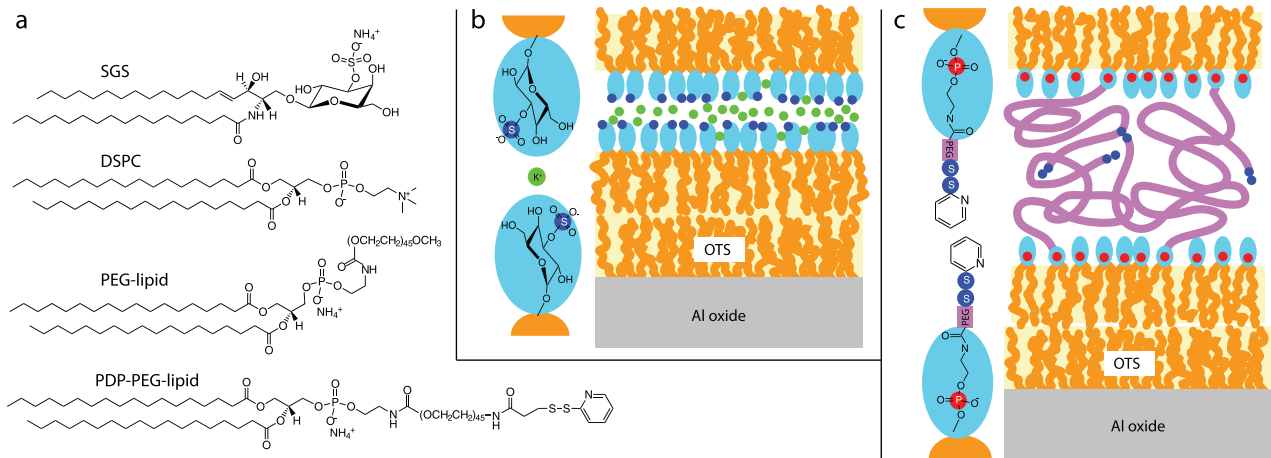


Figure 1. (a) Chemical structures of the amphiphilic molecules SGS (3-O-sulfo-D-galactosyl-β-1'-N-heptadecanoyl-D-erythro-sphingosine), DSPC (1,2-distearoyl-*sn*-glycero-3-phosphocholine), PEG-lipid (1,2-distearoyl-*sn*-glycero-3-phosphoethanolamine-N-[methoxy(polyethylene glycol)-2000]), and PDP-PEG-lipid (1,2-distearoyl-*sn*-glycero-3-phosphoethanolamine-N-[PDP(polyethylene glycol)-2000]). (b) and (c) Schematic illustration of the double-monolayer samples investigated in the present study. (b) Interacting SGS surfaces bearing S atoms (dark blue dots) in the lipid headgroups. Green dots indicate K⁺ counter ions. (c) Interacting lipid-anchored PEG brushes bearing P atoms (red dots) in the lipid headgroups and S atoms at the end of the PEG chains. The solid surfaces are hydrophobically functionalized with octadecyltrichlorosilane (OTS).

surface separation or (equivalent) water layer thickness D_w . For fixed temperature T and ambient pressure p , Π represents the derivative of the Gibbs free energy G per unit area A with respect to D_w [12],

$$\Pi(D_w) = -\frac{1}{A} \left(\frac{dG}{dD_w} \right)_{T,p}. \quad (1)$$

Pressure–distance relations are commonly determined by subjecting multilamellar stacks of interacting surfaces to dehydrating pressures of known magnitude [13]. So-called equivalent pressures can be exerted either by bringing the multilayers into contact with osmotically active polymer solutions, or by controlling the ambient relative humidity h_{rel} , in which case

$$\Pi(h_{rel}) = -\frac{k_B T}{v_w} \ln(h_{rel}), \quad (2)$$

where v_w denotes the volume of a water molecule and k_B is the Boltzmann constant. For biologically or technologically relevant ‘soft’ interfaces, the interaction characteristics are often closely related to molecular conformations and charge distributions [3]. For instance, forces between surfaces displaying charged chemical moieties depend on the exact location of the charges and on their ability to spatially rearrange upon the surfaces’ mutual approach. Similarly, electrostatic interactions between charged surfaces are sensitive to the distribution of counterions on the axis perpendicular to the surface plane [14]. Polymer-decorated surfaces, on the other hand, interact differently if the opposing polymer layers are able to overlap [15]. In other words, structural aspects like molecular conformations or element distributions are indicative of the interaction mechanisms and thus of great relevance. However, insight into structures ‘buried’ between two surfaces is difficult to obtain experimentally. X-ray and neutron scattering are among the very few techniques that

can probe such structures with the required sub-nanometer spatial resolution. Specular reflectometry reveals matter density profiles perpendicular to an interface [16, 17]. The latter can then be interpreted in terms of interfacial distributions of chemical components [18, 19]. This approach has been taken also to investigate the structure of lipid layers incorporating lipopolymers [20, 21] and of interacting soft interfaces [22–24]. However, it is not always possible to deduce the relevant structural features from such ‘global’ density profiles. In contrast, x-ray fluorescence allows determining element-specific density profiles across an interface [25]. The technique is based on the characteristic fluorescence induced by the illuminating x-rays via photoelectric ionization and has commonly been used to study element distributions at gas/liquid interfaces [26–28]. Ångstrom resolution perpendicular to the interface can be achieved with x-ray fluorescence under Bragg diffraction or mirror reflection conditions. In particular, planar nanometer-thick multilayers allow to create strongly modulated standing x-ray waves above the multilayer surface, whose period can be adjusted to match the typical length scales of the objects investigated [29, 30]. Such standing-wave x-ray fluorescence (SWXF) studies have so far dealt with the fluorescence of comparatively heavy elements, often used as labels [25]. Only recently we have established a label-free implementation of SWXF, which is suited to directly localize lighter and biologically relevant chemical elements like P and S with atom scale precision [31].

In the present work, we utilize this technique for the label-free element-specific structural investigation of interacting layers approximately mimicking the surfaces of distinct types of biological membranes. Measurements were carried out at varying humidity corresponding to different equivalent interaction pressures and surface separations. The results are discussed with respect to the pressure–distance curves of the same systems, which were determined in the present work by ellipsometry.

2. Results

Figures 1(b) and (c) schematically illustrate the studied double monolayer samples composed of the amphiphilic molecules shown in figure 1(a). They act as defined models of interacting membrane surfaces with known composition. Interacting surfaces composed of the glycolipid (SGS) (figure 1(b)) represent interacting membranes that contain significant densities of negatively charged sulfoglycolipids, like photosynthetic membranes [32]. Each SGS molecule (figure 1(a)) comprises one S atom that can be targeted by SWXF. These highly charged models of membrane surfaces are also suited to study the behavior of counterions. Here, the samples were prepared such that the counterions are K^+ ions (see section 4) that can also be localized with the SWXF settings employed. Interacting lipid-anchored PEG brushes (formed by 10 mol% lipopolymers anchored into a DSPC matrix, see figure 1(c)) in a generic way represent interacting membrane surfaces displaying hydrophilic macromolecules, such as cell glycocalyx [33], or the outer LPS surfaces of Gram-negative bacteria [8]. SWXF allows localizing the P atoms in DSPC and the lipopolymers (PEG-lipid or PDP-PEG-lipid) and the S atoms in the labeled polymer endpoints of PDP-PEG-lipid (figure 1(a)). With that, this system is uniquely suited for the simultaneous localization of the grafting surface (via its P content) and the endpoints of the brush (via its S content). Such architectures are therefore interesting also in context with a validation of theoretical models describing the conformation of interacting polymer brushes [34].

Double-monolayer architectures like the ones illustrated in figures 1(b) and (c) have similarities with commonly studied supported membranes (the solid support [35]) and lipid monolayers at the air/water interface (the vapor phase [20]). Importantly, they enable the controlled interaction of well-defined surfaces and the simultaneous hydration-dependent structural investigation. Since the amphiphilic monolayers are flexible, a homogeneous surface separation on the planar substrate is always realized, even if impurities, for example dust particles, locally perturb the interaction. This is in contrast to approaches involving two planar solids, where creation of a defined interaction distance is generally challenging [36]. Moreover, double monolayers can be used also for the study of non-symmetrical interaction scenarios and for molecular compositions that do not lead to the spontaneous formation of lamellar phases. This is in contrast to the classical multilayer swelling approach [37]. The interaction strength can be quantified in terms of the equivalent interaction pressure, which is dictated by the humidity (see equation (2)). The absence of bulk water serves for the controlled dehydration and is therefore desired. For high humidities close to saturation ($h_{\text{rel}} \rightarrow 100\%$), the samples are highly swollen and comprise a large amount of water corresponding to a large equivalent water layer thickness $D_w = v_w N_w / A$, where N_w is the number of water molecules per unit area A . Under this condition the surfaces are further apart than for low humidities, where the samples are less swollen and D_w is smaller.

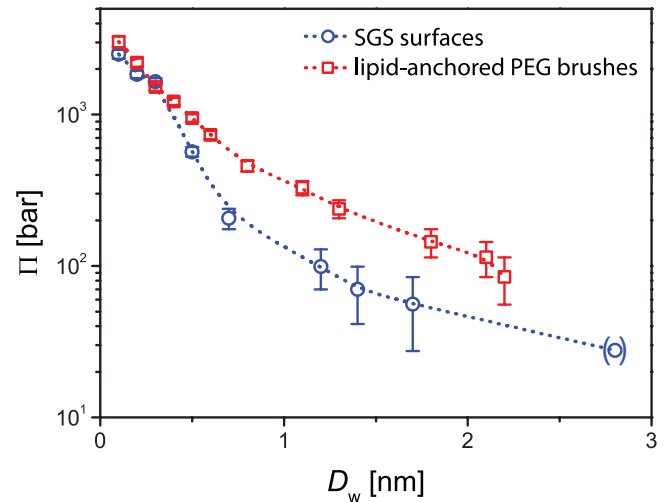


Figure 2. Pressure–distance curves of interacting SGS surfaces (circles) and lipid-anchored PEG brushes (squares). Error bars represent the uncertainty of the humidity sensor. For the data point in brackets the error in Π is comparable to its value. Dashed lines serve to guide the eye.

2.1. Pressure–distance curves

Figure 2 shows the pressure–distance curves of interacting SGS surfaces and lipid-anchored PEG brushes as determined by ellipsometry (see section 4). For both systems the interaction pressures are repulsive, meaning that work has to be performed in order to reduce D_w . Close to completely dehydrated conditions ($D_w \rightarrow 0$) the pressures reach magnitudes of several kbars. Upon reducing the equivalent pressure (i.e. increasing the humidity) to the lowest levels achieved in the present work, both systems take up a substantial amount of water, $D_w > 2$ nm. But despite these similarities, the repulsion mechanisms leading to water uptake upon releasing the equivalent pressure have to be considered totally different: The repulsion between the negatively charged SGS surfaces is mainly of electrostatic nature. As was shown recently, the range of the repulsive force between glycolipid surfaces increases substantially when negatively charged sulfoglycolipids are incorporated [32]. In contrast, charges play only a minor role for the repulsion between the lipid-anchored PEG brushes. Instead, the hydration of the polymer chains, as well as steric forces related to their configurational entropy are more important. While pure DSPC surfaces like other phosphatidylcholine (PC) lipid surfaces merely experience short range hydration repulsion [37, 38], the incorporation of PEG-lipid was shown to induce additional steric repulsion that systematically increases with polymer length and grafting density [39].

2.2. Element concentration profiles

Figure 3(a) illustrates the geometry of the SWXF experiments. The technique is based on the element-characteristic fluorescence induced via photoelectric ionization by a standing x-ray wave. The angle of incidence is denoted with θ . Close to the

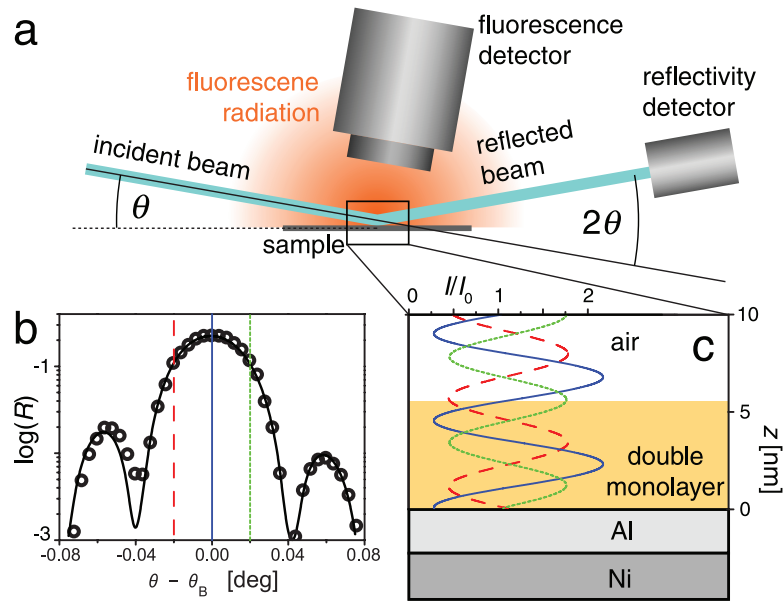


Figure 3. (a) Sketch of the SWXF measurement setup. Incident and reflected x-ray beams are indicated with bright blue lines. The isotropically emitted x-ray fluorescence radiation is indicated in red. The incident angle is denoted with θ . (b) Measured reflectivity curve (symbols) in the vicinity of the first Bragg angle θ_B of the solid multilayers and theoretical model (solid black line). (c) SW intensity patterns $\Phi(\theta, z)$ above the solid surface computed for $\theta = \theta_B$ (solid dark blue line) and for $\theta = \theta_B \pm 0.02^\circ$ (dotted green and dashed red lines, respectively), corresponding to the vertical lines in panel (b). The axis perpendicular to the planar solid surface is denoted with z . The region shaded in orange schematically represents the supported monolayer architectures.

Bragg angle θ_B of the multilayer substrate (here: $\theta_B = 1.13^\circ$), strong reflection occurs, giving rise to a highly modulated standing wave (SW) intensity pattern. Figure 3(b) (symbols) shows the intensity of the reflected beam in a narrow interval of $\pm 0.08^\circ$ around θ_B . The solid line represents the theoretically modeled reflectivity based on a suitable layer representation of the electron density profile of the periodic Al/Ni layers (see section 4). The θ -dependent fluorescence intensity of a target element j , $I_j(\theta)$, scales with a spatial integral containing the elemental concentration profile perpendicular to the interface, $c_j(z)$, and the θ -dependent SW intensity $\Phi(\theta, z)$:

$$I_j(\theta) = A \int_{-\infty}^{\infty} \Phi(\theta, z) c_j(z) dz, \quad (3)$$

where A is a pre-factor that involves, among others, fluorescence yield, beam footprint, and detector field-of-view, and therefore weakly depends on θ in general [31]. According to equation (3), $c_j(z)$ can thus be deduced from $I_j(\theta)$, if $\Phi(\theta, z)$ is known. The latter was computed via the phase-correct summation of all reflected and transmitted partial waves [28] from the layer representation mentioned above. For illustration, calculated SW intensity patterns $\Phi(\theta, z)$ above the solid surface are shown in figure 3(c) for $\theta = \theta_B$ and for $\theta = \theta_B \pm 0.02^\circ$ (see vertical lines in figure 3(b)). As θ is increased through the Bragg condition, the nodes and antinodes of the SW intensity shift towards the solid surface by approximately half a multilayer period.

Fluorescence spectra were measured for various incident angles in θ -scans around the Bragg angle. Figure 4 shows a representative spectrum of interacting lipid-anchored PEG brushes (see figure 1(c)), recorded exemplarily for $\theta = \theta_B$. The spectrum exhibits the characteristic fluorescence peaks of P and S (see inset) together with peaks of Al and other chemical elements found in the multilayer substrates and in the

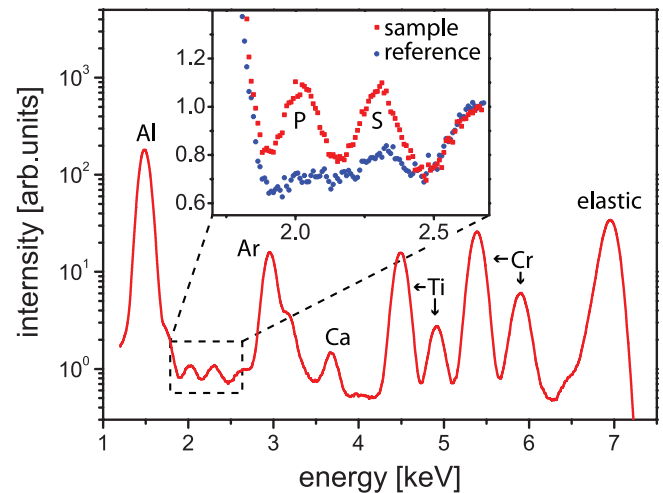


Figure 4. X-ray fluorescence spectrum of interacting lipid-anchored PEG brushes (see figure 1(c)) recorded exemplarily for $\theta = \theta_B$. The spectrum comprises characteristic peaks of Al and other chemical elements found in the multilayer substrates and in the sample environment (Ar, Ti, and Cr). Inset: characteristic fluorescence peaks of P and S. Unlike the main panel the inset also shows the comparison with the reference spectrum obtained in the absence of the P and S loaded double monolayer.

sample environment (Ar, Ti, and Cr). Ni does not emit fluorescence because the incident beam energy is below the K-shell edge of Ni. The fluorescence intensities of the target elements were extracted from the spectra for each incident angle. For this purpose, from the sample spectra the corresponding reference spectra of the substrates in the absence of the interacting monolayers were subtracted. The peaks of the target elements in the resulting difference spectra were then modeled with Gaussian functions, and the obtained amplitudes were used

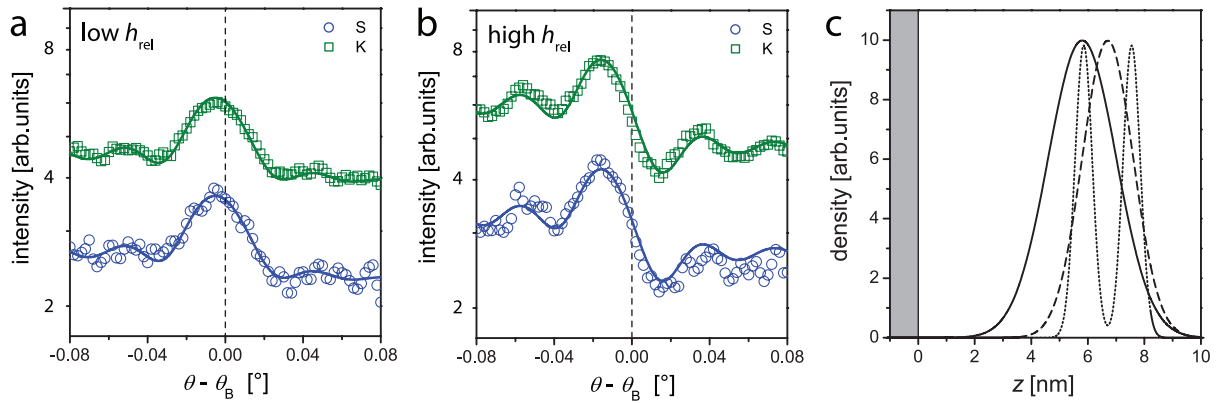


Figure 5. (a) Angle-dependent S and K fluorescence (symbols) from interacting SGS surfaces (see figure 1(b)) at low humidity. (b) S and K fluorescence from the same sample but at high humidity. Solid lines in (a) and (b) indicate calculated theoretical intensities corresponding to the best-matching model parameters for the S distributions at low and high humidity. (c) S distributions at low humidity (solid line) and at high humidity when assuming unimodal shape (dashed line). The dotted line indicates a bimodal distribution that would result in approximately the same fluorescence signals (see text). The K distributions at low and high humidity are undistinguishable from the respective S distributions, so that the curves in panel (c) apply to both S and K.

to build for each element its θ -dependent fluorescence intensity curves $I_f(\theta)$. In the last step, based on the known shape of $\Phi(\theta, z)$, the intensities curves were modeled according to equation (3) using a suitable parameterization of the element profiles $c_f(z)$. The weak angle-dependence of the pre-factor A in the equation was approximated linearly with an adjustable parameter for the slope, as was done in [31].

2.2.1. Interacting SGS surfaces. Figure 5(a) (bottom curve, symbols) shows the angle-dependent S fluorescence, $I_S(\theta)$, of interacting SGS surfaces (figure 1(b)) at a low humidity of $h_{rel} \approx 50\%$, corresponding to $\Pi \approx 1$ kbar (equation (2)). As suggested by the pressure distance curve (figure 2, circles), under strongly dehydrating conditions the water layer between the two sulfur-bearing surfaces is only few Å thick, comparable to the surface roughness. The S distributions belonging to the two surfaces are therefore expected to strongly overlap, resulting in an overall S distribution with only one maximum. The S concentration profile $c_S(z)$ was accordingly modeled as a unimodal distribution,

$$c_S(z) = c_{max} e^{-(z-z_S)^2/(2\sigma_S^2)}. \quad (4)$$

In this Gaussian representation, the amplitude c_{max} , the center position z_S and the width σ_S are adjustable fitting parameters. While c_{max} merely acts as a scaling parameter, z_S is linked to the angular positions of the extrema in $I_S(\theta)$ and the total form of the curve. The width σ_S is mostly defined by the relative amplitude of the modulation of $I_S(\theta)$ with respect to the ‘baseline’ further away from θ_B . The solid line superimposed to the data points represents the theoretical S fluorescence curve, calculated according to equation (3) for the best matching parameters, $z_S = 72$ Å and $\sigma_S = 12$ Å. It is seen that the unimodal distribution reproduces the experimental data points well. The obtained center of mass position, $z_S = 72$ Å above the solid surface is based on the assumption that all the metal layers are 24 Å thick, as calculated from the reflectivity data (see section 4.5), including the uppermost Al and Ni layers. One should expect, however, that the terminal layers are at least partially oxidized and therefore significantly thicker [40, 41],

so that the actual surface is shifted along the z -axis. In a previous study in which the surface position had been calibrated on an absolute scale, the center of mass distribution of S in a similar sample at uncontrolled humidity was found at around 58 Å above the surface [31]. In order to be consistent with this value, a thickening of the terminal metal layers of 14 Å by oxidation has to be assumed, which appears plausible. With this definition of the z -axis, which will be used in the following, $z_S = 58$ Å is obtained. The corresponding concentration profile is shown in figure 5(c) as a solid line. The obtained width of the distribution, $\sigma_S = 12$ Å, at first sight seems to reflect the topographic roughness of solid substrate ($\sigma_{top} \approx 11$ Å, see section 4). In that case the S distribution could be interpreted as a negligibly thin layer ideally following the corrugations of the solid surface. However, the topographic roughness effectively ‘seen’ by SWXF corresponds to mesoscopic in-plane length scales and can thus be significantly smaller than the one probed by atomic force microscopy (AFM) on the micrometer scale. Moreover the deformable organic layers do not necessarily fully follow these corrugations. Instead, they can have lower topographic roughness due to their considerable interfacial tension. In both cases σ_S would additionally reflect the intrinsic width of the S distribution, also in terms of its inherent bimodal nature. The upper curve in figure 5(a) (symbols) shows the angle-dependent K fluorescence, $I_K(\theta)$, under the same low-humidity conditions. It exhibits the essentially identical angle dependence as $I_S(\theta)$, and can thus be described satisfactorily with the same parameters (see solid line superimposed to the data points), apart from the trivial scaling parameter c_{max} . In other words, S and K distributions almost perfectly overlap, so that the solid line in figure 5(c) also describes the K distribution. This co-localization indicates that the counter-ions are always found in the immediate vicinity of the negatively-charged sulfate groups of SGS.

Figure 5(b) (bottom curve, symbols) shows $I_S(\theta)$ for interacting SGS surfaces at a high humidity of $h_{rel} \approx 93\%$, corresponding to $\Pi \approx 100$ bar (equation (2)). Its angle-dependence is very different from that observed at low humidity, reflecting a significant shift of the S distribution further away from the

solid surface. In fact, the data points for high humidity can still be described satisfactorily with a unimodal distribution (equation (4)), see superimposed solid line for $z_S = 67$ Å and $\sigma_S = 9$ Å. The corresponding concentration profile is shown in figure 5(c) as a dashed line. This is at first surprising, because the S distributions belonging to the two sulfur-bearing surfaces are expected to separate for thicker water layers, resulting in a bimodal overall S distribution. The unimodal description however still works, because SWXF is sensitive mainly to the first and second moments of a narrow elemental distribution, $z_j = \langle z \rangle$ and $\sigma_j^2 = \langle (z - z_j)^2 \rangle$, respectively [31], an aspect that will be discussed further below. First we notice that the shift in z_S when going from low to high h_{rel} is $\delta z = 9$ Å. Assuming that the center of the S distribution belonging to the proximal SGS monolayer is hydration-independent, the S distribution belonging to the distal monolayer would have to shift by $2\delta z = 18$ Å to give the same effect. This extent of swelling upon changing the equivalent pressure from $\Pi \approx 1$ kbar to $\Pi \approx 100$ bar is in rough agreement with the pressure–distance curve of interacting SGS monolayers (figure 2). Coming back to the precise shape of the S distribution at high humidity, we note that the S fluorescence data in figure 5(b) are also consistent with a more plausible, bimodal distribution, provided that it exhibits approximately the same first and second moments of the unimodal distribution used to fit the data. As shown in the supporting information (stacks.iop.org/JPhysD/50/104001/mmedia), deviations from this approximation are negligible. A symmetrical bimodal distribution, centered around z_j and comprising two Gaussian peaks of individual width σ_{ind} , separated by a distance Δz , has the same first moment as the unimodal distribution. For the second moment we have $\sigma_{bimod}^2 = (\Delta z/2)^2 + \sigma_{ind}^2$. When σ_{bimod} is set equal to the width σ_S obtained for the unimodal distribution, we can solve for Δz , which is then only a function of σ_{ind} , $\Delta z = 2\sqrt{\sigma_S^2 - \sigma_{ind}^2}$. The dotted line figure 5(c) shows an exemplary bimodal distribution with compatible first and second moments as obtained for a very low value of the individual peak width, $\sigma_{ind} = 3$ Å. The upper curve in figure 5(b) (symbols) shows the angle-dependent K fluorescence, $I_K(\theta)$, under the same high-humidity conditions. Again, it has the same angle dependence as $I_S(\theta)$, indicating perfect overlap of S and K distributions. This result suggests that, even under highly hydrated conditions the counterions reside closely to the negatively charged surfaces, rather than being evenly distributed in the aqueous phase.

Both the shift in z_S and z_K upon increasing the humidity and the agreement of a bimodal distribution with the experimental data are consistent with the expected swelling behavior of the architecture illustrated in figure 1(b). However, it is difficult to rationalize why the second moment of the S distribution does not become larger with increasing hydration level. This behavior may have to do with a more effective healing of the corrugations of the solid surface by the organic layers when they are highly hydrated. In addition one may expect that the saccharide headgroups of SGS undergo significant reorientation with increasing hydration, such that the S atoms get more directed towards the center of the aqueous layer. Alternatively,

our experimental results may suggest that the SGS double-monolayers undergo more substantial architectural changes with changing hydration level.

2.2.2. Interacting lipid-anchored PEG brushes. Figure 6(a) (bottom curve, symbols) shows the angle-dependent P fluorescence, $I_P(\theta)$, of interacting lipid-anchored PEG brushes at a low humidity of $h_{rel} \approx 40\%$, corresponding to $\Pi \approx 1.3$ kbar (equation (2)). Even under such dehydrating conditions we expect a clearly bimodal P distribution due to the presence of the PEG layer between the surfaces of the phosphorus-bearing lipid matrix (figure 1(c)). Moreover, the maxima of the distribution may exhibit a separation comparable to the SW period above the solid surface $\Lambda = 45$ Å (due to refraction effects Λ is not exactly identical to the multilayer period of 48 Å). In this case more than one oscillation of the SW contributes to the fluorescence, an effect that imparts some ambiguity to the data. In fact, $I_P(\theta)$ can readily be reproduced with a unimodal Gaussian distribution with $z_P = 57$ Å and $\sigma_P = 10$ Å, as indicated with the solid line superimposed to the data points. But due to the discrete translational invariance of the SW, the same theoretical curve is obtained for a bimodal distribution with an additional, identical Gaussian peak at $z_P' = z_P + \Lambda = 102$ Å. This bimodal P distribution, which qualitatively is a plausible description of the sample architecture, is shown in figure 6(c) (upper part, solid line). We remark, however, that on top of this two-fold ambiguity there is also another level of ambiguity with respect to details of the individual Gaussian distributions. Namely, the effective width, $\sigma_P = 10$ Å, obtained when assuming a unimodal distribution would also result from a bimodal distribution of sharper peaks that are separated by few Å more or less than Λ . However, since the width obtained ($\sigma_P = 10$ Å) is already rather low, about as low as σ_{top} , we assume that this ambiguity is of minor relevance and the P distribution plotted in figure 6(c) provides a satisfactory description of the sample structure. This conclusion is also corroborated by the fact that the position of the proximal P peak in the interacting PEG brushes ($z_P = 57$ Å) is consistent with the center of the S distribution of the dehydrated SGS double-monolayer ($z_S = 58$ Å) in light of the similar sample architecture up to the proximal lipid monolayer.

The upper curve in figure 6(a) (symbols) shows the angle-dependent S fluorescence, $I_S(\theta)$, under the same low-humidity conditions. The fluorescence, originating from S atoms in the PDP-labeled end-points of the PEG chains (figure 1(a)), assumes a maximum at a significantly larger angle than $I_P(\theta)$ in the same plot, reflecting that P and S have strongly dissimilar distributions. $I_S(\theta)$ is well reproduced for a slightly broader, unimodal distribution with $\sigma_S = 13$ Å, located between the two peaks of the P distribution. The best match with the data points is achieved with $z_S = 88$ Å, see superimposed solid line. The corresponding S distribution is shown in figure 6(c) (upper part) as a dashed line. The P and S distributions in figure 6(c), representing brush grafting surfaces and polymer endpoints, obviously do not match the expected symmetry of the sample architecture, where z_S would ideally coincide with the center between the two P peaks at $z = 80$ Å. In view of the above-discussed considerable uncertainties in

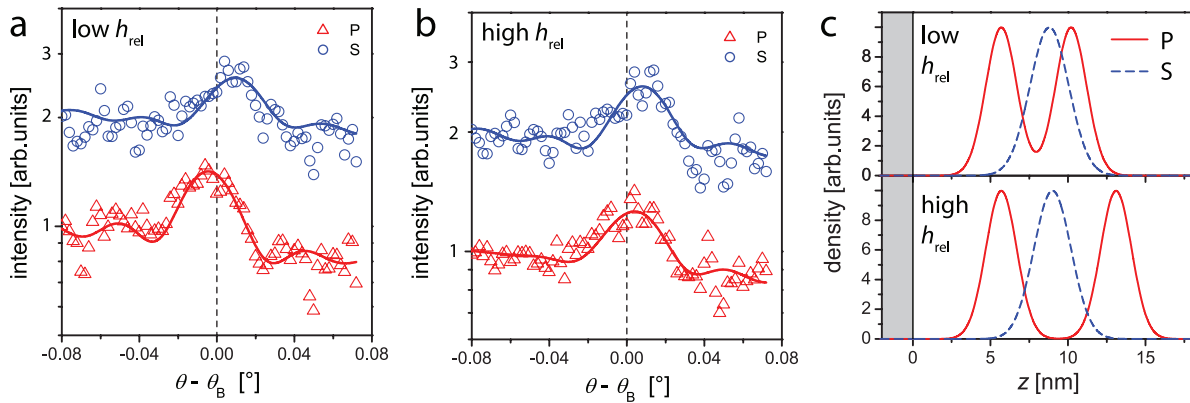


Figure 6. (a) Angle-dependent P and S fluorescence (symbols) from interacting lipid-anchored PEG brushes (see figure 1(c)) at low humidity. (b) P and S fluorescence from the same sample but at high humidity. Solid lines in (a) and (b) indicate calculated theoretical intensities corresponding to the respective model parameters for P and S distributions at low and high humidity. (c) P (solid line) and S (dashed line) distributions at low humidity (upper part) and at high humidity (lower part).

the interpretation of the fluorescence intensities, it is difficult to conclude whether the observed asymmetry is significant, in which case it could reflect, for instance, differences in the packing densities of proximal and distal monolayers.

Figure 6(b) (bottom curve, symbols) shows $I_P(\theta)$ for the interacting PEG brushes at a high humidity of $h_{rel} \approx 94\%$, corresponding to $\Pi \approx 80$ bar (equation (2)). According to the pressure–distance curve in figure 2, swelling by $\gtrsim 2$ nm is expected when reducing the equivalent pressure to this level. A significant change in the P distribution is also evidenced by $I_P(\theta)$, in which the feature-to-baseline level is significantly reduced while the maximum is shifted almost exactly to θ_B at high humidity. An angle dependence like the one obtained for the P fluorescence at high humidity is characteristic for element profiles that are rather equally distributed over the nodes and antinodes of the SW, indicating that the distance between the peaks in a bimodal distribution is closer to an odd than to an even multiple of $\Lambda/2$. Indeed, as indicated with the solid line superimposed to the data points, $I_P(\theta)$ is well reproduced when the distal peak in the bimodal P distribution is shifted to $z_{P'} = 131$ Å by 29 Å, which is only a fraction of Λ . This shift is also roughly consistent with the swelling observed in the pressure–distance curve of the PEG brushes. The corresponding P distribution is shown as a solid line in the lower part of figure 6(c). We remark that the experimental data are reproduced even slightly better when the position of the proximal peak is also allowed to move, in which case it moves towards the solid surface by 2 Å (not shown). The upper curve in figure 6(b) (symbols) shows the angle-dependent S fluorescence, $I_S(\theta)$, under the same high-humidity conditions. Within the statistical noise of the data points there are no significant differences between $I_S(\theta)$ at low and high humidity, respectively. The best-matching unimodal S distribution at high humidity, corresponding to the solid line superimposed to the data points, has $\sigma_S = 12$ Å and $z_S = 90$ Å, the latter being close to the center between the two P peaks at $z = 94$ Å. The corresponding S (or end-point) distribution is shown as a dashed line in the bottom part of figure 6(c). The P and S distributions suggest that the symmetry of the double-monolayer architecture is recovered at higher humidity. Significant differences

in the packing densities of proximal and distal monolayers, as speculated above, are therefore not likely the reason for the asymmetry observed at low humidity. The end-point distribution in a single layer of tethered polymers has previously been determined by SWXF [42]. To our knowledge the present results constitute the first determination of the end-point distribution of confined, interacting polymer brushes.

3. Discussion and conclusions

In the preceding section we have demonstrated that double-monolayer architectures like the ones illustrated in figures 1(b) and (c) are well suited for a comprehensive investigation of interacting well-defined surfaces. Namely, such architectures enable the simultaneous determination of pressure–distance curves and of structural details, for example by using x-ray or neutron scattering techniques. We have further demonstrated that SWXF is suited for the label-free and element specific structural investigation of interacting layers. When resolved with high resolution, elemental distributions can yield accurate insight into the molecular configuration of interacting surfaces and its response to changes in the surface separation. In fact, our results suggest that such information is conveniently obtained when elemental distributions are unimodal, for instance when the interacting surfaces have different composition. In many configurations, like the ones described in the present work, the relevant elemental distributions are however multimodal. In these cases detailed molecular conformations are only accessible when the shape of the multimodal distributions can be determined unambiguously. To this end, the topographic roughness of the solid surface poses a limitation, because it leads to a smearing out of the elemental profiles, thus reducing the structural detail. Secondly, ambiguity occurs especially when the distances between the distribution maxima are comparable to the SW period. As a consequence, the structural information obtained from the particular set of measurements presented here does not go much beyond what one could also obtain using conventional reflectometry. Nonetheless, our results constitute a proof-of-concept and clearly demonstrate the potential of SWXF when the crucial

parameters are optimized: The roughness-induced smearing out of elemental distributions can be avoided by using multilayer substrates with very smooth surfaces [31]. Ambiguities related to multimodal distributions can be overcome by involving *ab initio* information about the sample structure, as well as by a suitable choice of multilayer periods or by working with multiple angle ranges, e.g. in total reflection and with two sufficiently intense Bragg peaks. One can also consider an experiment with similar samples on two ML substrates of different period. Even in the most unfavorable case of a ML period matching exactly the peak distance in a bimodal distribution the results stay very sensitive to the changes in the key distribution parameters. Finally, x-ray reflectivity measurements, carried out in parallel on samples of identical composition but supported by simple solids like sapphire or silicon can yield valuable complementary structural information facilitating the interpretation of the x-ray fluorescence data. With that, SWXF may reveal distinct structural aspects not only of generic interactions between soft interfaces but also of specific membrane–membrane interactions for which only the forces have been quantified so far [43, 44].

4. Materials and methods

4.1. Materials

Unless stated otherwise, all chemicals were purchased from Sigma (St. Louis, MO, USA) and used without further purification. Water was purified and double-deionized (MilliQ, Molsheim, France). Sulfoglycolipids (SGS), phospholipids (DSPC), and lipopolymers (PEG-lipid and PDP-PEG-lipid) were purchased from Avanti Polar Lipids (Alabaster, AL, USA). As illustrated in figure 1(a), SGS (3-O-sulfo-D-galactosyl- β 1-1'-N-heptadecanoyl-D-erythro-sphingosine) has two hydrophobic fatty acid tails and a sulfated galactose monosaccharide headgroup. At neutral pH the sulfate carries one negative charge. DSPC (1,2-distearoyl-*sn*-glycero-3-phosphocholine) has two all-saturated C₁₈ chains and a zwitterionic phosphocholine headgroup which carries one P atom. PEG-lipid (1,2-distearoyl-*sn*-glycero-3-phosphoethanolamine-N-[methoxy(polyethylene glycol)-2000]) is similar to DSPC but a PEG chain comprising 46 monomers is covalently attached to the headgroup. In PDP-PEG-lipid (1,2-distearoyl-*sn*-glycero-3-phosphoethanolamine-N-[PDP(polyethylene glycol)-2000]), the terminus of the PEG chain is covalently functionalized with a pyridyldithiopropionate (PDP) moiety containing two S atoms. Multilayer substrates were purchased from X'scitech (Helsinki, Finland) and had 25 repetitions of Al(2.4 nm)/Ni(2.4 nm) alternating layers on top of sapphire single crystal wafers with dimensions 8 mm \times 8 mm \times 1 mm. The terminal Al layer forms amorphous aluminum oxide at the outer surface. AFM was used to reveal the topography of the outer surface and in particular its root-mean-square (rms) roughness, $\sigma_{\text{top}} \approx 11$ Å. Silicon wafers (150 mm diameter, 625 μ m thickness) with a thermal oxide of defined thickness were purchased from SIEGERT Wafer GmbH (Aachen, Germany).

4.2. Sample preparation

Silicon wafers were cut into pieces of 17 mm \times 12 mm. Multilayer substrates and silicon substrates were cleaned by washing with chloroform, acetone, ethanol, and water, followed by UV-ozone treatment. The surfaces were then rendered hydrophobic via covalent functionalization with OTS by immersion in 1 mM OTS solutions in anhydrous hexadecane for 1 h and subsequent rinsing in hexadecane and ethanol. SGS, DSPC, and the lipopolymers PEG-lipid and PDP-PEG-lipid were dissolved in chloroform at 2 mg ml⁻¹. To obtain DSPC/lipopolymer mixtures at a lipopolymer mole fraction of 10 mol%, DSPC solution was mixed with PEG-lipid or PDP-PEG-lipid solution, respectively. Double monolayers of SGS or DSPC/lipopolymer on the surfaces multilayer substrates or silicon substrates were prepared using a combination of the Langmuir–Schaefer (LS) and Langmuir–Blodgett (LB) transfer methods [45]. For this purpose, chloroform solutions of SGS or DSPC/lipopolymer mixtures were first spread at the air/water interface in a Langmuir trough (Nima Technology, Coventry, UK; or Riegler & Kirstein GmbH, Potsdam, Germany) containing 1 mM KBr aqueous solution (for SGS) or pure water (for DSPC/lipopolymer mixtures). The amphiphilic molecules immobilized at the interface were then compressed to a monolayer with a lateral pressure of 35 ± 1 mN m⁻¹. A first lipid layer was deposited onto the hydrophobically functionalized surfaces via LS transfer, i.e. with the solid surface facing the water surface. This procedure reproducibly yields transfer ratios close to 100%, as evidenced from the negligibly small variation of the surface pressure upon the initial contact and as previously confirmed by neutron reflectometry [19]. In the next step the solid substrate was rotated under water by 90°, so that its surface ended up perpendicular to the water surface. The remaining lipid monolayer at the air/water interface was then removed and replaced with a fresh monolayer at the same lateral pressure. This second monolayer was then transferred on top of the first layer by LB, i.e. by pulling the solid substrate upwards. The LB transfer was confirmed to be effective and reproducible by ellipsometry (see section 4.3. and supporting material).

4.3. Ellipsometry measurements

Ellipsometry enables the characterization of interfacial layers in terms of refractive indices and thicknesses. The method is based on the change in the polarization state of light upon reflection from the surface. For a given refractive index n , the change depends on the layer thickness and is quantified in terms of the phase difference Δ and the amplitude ratio Ψ encoded in the ratio between the complex reflection coefficients R_s and R_p for s and p polarizations, respectively [46]:

$$R_p/R_s = \tan \Psi e^{-i\Delta}. \quad (5)$$

For ellipsometry measurements, silicon chips with thermal oxide were used as substrates for the double monolayers. Silicon has the complex refractive index $n_{\text{Si}} = 3.885 - 0.018i$ [47]. Measurements were conducted at an incident angle of 70°, with an Optrel Multiskop ellipsometer working with a

wavelength $\lambda_{\text{elli}} = 632.8 \text{ nm}$. For the known refractive index of SiO_2 , $n_{\text{SiO}_2} = 1.456$ [48], the obtained measurement values ($\Delta = 79.3^\circ$, $\Psi = 44.3^\circ$) correspond to an oxide layer thickness of 105.5 nm, close to the nominal value of 100 nm. In the next step, the measurement values obtained for the fully dehydrated ($h_{\text{rel}} < 5\%$) samples were modeled with an additional single layer for the organic film comprising OTS and the two deposited monolayers in order to obtain their thicknesses in the absence of water. In this procedure, the refractive index of the organic film was assumed as $n_{\text{org}} = 1.46$, a typical value for organic materials [49–51]. The obtained layer thicknesses exhibit excellent proportionality to the nominal material amount deposited, see supporting material. In the last step, the measurement values obtained at controlled humidity were modeled with an additional water layer ($n_{\text{wat}} = 1.33$) while accounting for the known optical parameters of oxide and dry organic layers. In this way, the humidity-dependent equivalent thickness of the water layer $D_w(h_{\text{rel}})$ was determined. Humidity was controlled by placing the samples inside a closed chamber through which humidified N_2 was streamed. The gas was humidified by letting it pass through a temperature-controlled water bath in the form of mm-sized bubbles. High humidities were realized by elevating the water temperature to close to or even slightly above the sample temperature. Low humidities were realized either by lowering the bath temperature or by mixing the humidified N_2 stream with dry N_2 . The humidity at the sample position was measured with a calibrated humidity sensor (SHT75, Sensirion AG, Staefa, Switzerland) measurement uncertainty $\Delta h_{\text{rel}} = \pm 2\%$, placed close to the sample surface. The equivalent dehydrating pressure follows from h_{rel} according to equation (2).

4.4. X-ray experiments

X-ray specular reflectometry and SWXF experiments were carried out at the ID10 beamline of ESRF (Grenoble, France). The sample surface was oriented vertically. The beam was focused in vertical direction while its angular divergence was kept low in horizontal direction in order to obtain a near-parallel incident x-ray wave in the scattering plane. The latter is required to scan the Bragg reflection condition of the periodic metal multilayers with high angular resolution. The beam diameter was 40 μm horizontally and 500 μm vertically. For an illumination close to $\theta_B = 1.13^\circ$, the size of the beam footprint on the surface thus was 500 μm vertically and $\approx 2 \text{ mm}$ horizontally. The beam energy was 7.0 keV, corresponding to a wavelength of $\lambda = 1.77 \text{ \AA}$. The fluorescence radiation was measured using a silicon drift detector (Vortex-EM, SII NanoTechnology) placed perpendicular to the beam direction and about 3 mm from the surface. To improve measurement statistics without beam damage to the samples, the angular scans were repeated several times with vertically shifted beam position on the sample surface. In fact, when for test purposes the same position was scanned several times, no significant change in the signals was observed, suggesting that beam damage is negligible.

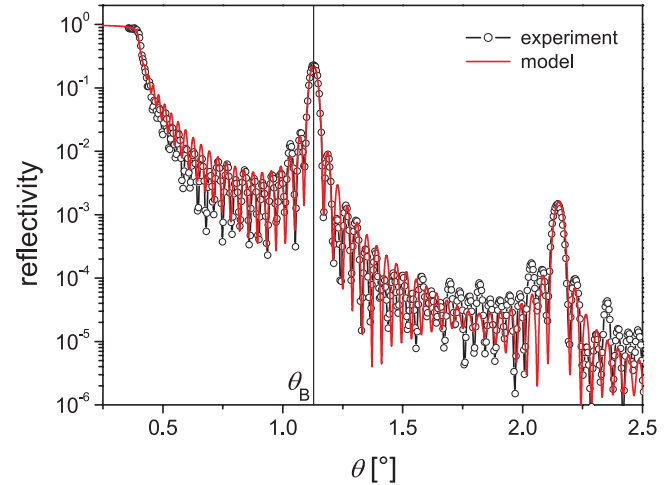


Figure 7. Measured reflectivity curve of a solid multilayer substrate (symbols) together with theoretical reflectivity (solid red line) calculated using a suitable electron density layer model of the periodic Al/Ni structure. The vertical straight line indicates the Bragg angle θ_B .

4.5. Layer representation of the periodic Al/Ni layers

Specular reflectometry from the bare multilayer substrates was measured in order to determine their layered structure, the latter being a prerequisite for accurately modeling the angle dependent SW intensity $\Phi(\theta, z)$. The reflectivity $R(\theta)$ denotes the θ -dependent ratio between the intensities of reflected and incident beams, respectively, and contains information on the electron density distribution perpendicular to an interface. Figure 7 shows $R(\theta)$ of a multilayer substrate in air, measured in θ - 2θ scans with a point detector placed at 2θ (see figure 2(a)). The substrate was functionalized with OTS, which owing to its weak electron density contrast (when compared to the solid metal layers) could be safely neglected in the reflectivity analysis. Experimental data (symbols) are corrected for the θ -dependent size of the beam footprint on the sample surface. The red solid line represents the theoretically modeled reflectivity based on a suitable layer representation of the periodic Al/Ni layers. It was computed from the layer representation via application of Fresnel's reflection laws at each interface and a phase-correct summation using the iterative recipe of Parratt [52]. The model assumes 25 periodic repetitions of alternating Al and Ni layers on top of a sapphire (Al_2O_3 , electron density $1.19 \text{ e}^- \text{ \AA}^{-3}$). Thickness and electron density of Al and Ni layers (d_{Al} , d_{Ni} , $\rho_{\text{Al}}^{\text{el}}$ and $\rho_{\text{Ni}}^{\text{el}}$, respectively) as well as their interfacial roughness were adjustable fitting parameters. The best-matching model parameters were obtained in a minimum χ^2 fit to the experimental data using the programs Motofit [53] and a web-based tool by Sergey Stepanov for reflectivity analysis [54]. The best match was obtained for $d_{\text{Al}} \approx d_{\text{Ni}} \approx 24 \text{ \AA}$ and $\rho_{\text{Al}}^{\text{el}} = 1.23 \text{ e}^- \text{ \AA}^{-3}$ and $\rho_{\text{Ni}}^{\text{el}} = 2.09 \text{ e}^- \text{ \AA}^{-3}$. All roughness parameters were found to be no larger than 10 \AA . It should be noted that $\rho_{\text{Al}}^{\text{el}}$ as obtained is about 50% higher than the literature value for pure Al ($0.80 \text{ e}^- \text{ \AA}^{-3}$), while $\rho_{\text{Ni}}^{\text{el}}$ is slightly lower (about 9%) than the literature value

for pure Ni ($2.29 \text{ e}^- \text{ \AA}^{-3}$), indicating that significant intermixing between Al and Ni layers occurs.

Acknowledgments

We thank Jean Daillant for insightful comments and Aurelio Barbetta and Anne Heilig for help with sample preparation and complementary AFM measurements, respectively. We acknowledge the European Synchrotron Radiation Facility for provision of synchrotron radiation facilities at beamline ID10. This work was financially supported by the Max Planck Society and by the German Research Foundation (DFG) via Emmy-Noether Grant SCHN1396/1.

References

- [1] Evans D F and Wennerström H 1994 *The Colloidal Domain—Where Physics, Chemistry, Biology, and Technology Meet* (New York: VCH)
- [2] Mouritsen O G 2005 *Life—As a Matter of Fat* (Berlin: Springer-Verlag)
- [3] Schneck E 2017 The interaction between soft interfaces: forces and structural aspects *Adv. Mater. Interfaces* **12** 1600349
- [4] Alberts B, Johnson A, Lewis J, Raff M, Roberts K and Walter P 2002 *Molecular Biology of the Cell* 4th edn (New York: Garland Science)
- [5] Eggens I, Fenderson B, Toyokuni T, Dean B, Stroud M and Hakomori S I 1989 Specific interaction between Lex and Lex determinants. A possible basis for cell recognition in preimplantation embryos and in embryonal carcinoma cells *J. Biol. Chem.* **264** 9476–84
- [6] Rosenhahn A, Schilp S, Kreuzer H J and Grunze M 2010 The role of ‘inert’ surface chemistry in marine biofouling prevention *Phys. Chem. Chem. Phys.* **12** 4275–86
- [7] Webb M S and Green B R 1990 Effects of neutral and anionic lipids on digalactosyldiacylglycerol vesicle aggregation *Biochim. Biophys. Acta* **1030** 231–7
- [8] Lau P C Y, Lindhout T, Beveridge T J, Dutcher J R and Lam J S 2009 Differential lipopolysaccharide core capping leads to quantitative and correlated modifications of mechanical and structural properties in *Pseudomonas aeruginosa* biofilms *J. Bacteriol.* **191** 6618–31
- [9] Bauer C, Bauduin P, Dufrière J F, Zemb T and Diat O 2012 Liquid/liquid metal extraction: phase diagram topology resulting from molecular interactions between extractant, ion, oil and water *Eur. Phys. J. Spec. Top.* **213** 225–41
- [10] Raviv U, Giasson S, Kampf N, Gohy J-Fo, Jérôme R and Klein J 2003 Lubrication by charged polymers *Nature* **425** 163–5
- [11] Lyklema H (ed) 2000 *Fundamentals of Interface and Colloid Science, Vol. 3: Liquid-Fluid interfaces* (London: Academic)
- [11] Lyklema H (ed) 2005 *Fundamentals of Interface and Colloid Science, Vol. 5: Soft Colloids* (London: Elsevier)
- [12] Derjaguin B V and Churaev N V 1987 *Surface Forces* (New York: Consultants Bureau)
- [13] Parsegian V A, Fuller N and Rand R P 1979 Measured work of deformation and repulsion of lecithin bilayers *Proc. Natl Acad. Sci.* **76** 2750–4
- [14] Israelachvili J N 1991 *Intermolecular and Surface Forces* 2nd edn (London: Academic)
- [15] Wijmans C M, Zhulina E B and Fleer G J 1994 Effect of free polymer on the structure of a polymer brush and interaction between two polymer brushes *Macromolecules* **27** 3238–48
- [16] Als-Nielsen J and McMorro D 2001 *Elements of Modern X-Ray Physics* (Chichester: Wiley)
- [17] Daillant J and Gibaud A 2009 *X-Ray and Neutron Reflectivity: Principles and Applications* (Berlin: Springer)
- [18] Helm C A and Als-Nielsen J 1987 Phospholipid monolayer density distribution perpendicular to the water surface. A synchrotron x-ray reflectivity study *Europhys. Lett.* **4** 697
- [19] Schneck E, Berts I, Halperin A, Daillant J and Fragneto G 2015 Neutron reflectometry from poly (ethylene-glycol) brushes binding anti-PEG antibodies: evidence of ternary adsorption *Biomaterials* **46** 95–104
- [20] Majewski J et al 1998 X-ray synchrotron study of packing and protrusions of polymer-lipid monolayers at the air-water interface *J. Am. Chem. Soc.* **120** 1469–73
- [21] Kuhl T L et al 1998 A neutron reflectivity study of polymer-modified phospholipid monolayers at the solid-solution interface: polyethylene glycol-lipids on silane-modified substrates *Biophys. J.* **75** 2352–62
- [22] Hamilton W A, Smith G S, Alcantar N A, Majewski J, Toomey R G and Kuhl T L 2004 Determining the density profile of confined polymer brushes with neutron reflectivity *J. Polym. Sci. B* **42** 3290–301
- [23] Mulder D J and Kuhl T L 2010 Polymer brushes in restricted geometries *Soft Matter* **6** 5401–7
- [24] Guenoun P, Schalchli A, Sentenac D, Mays J W and Benattar J J 1995 Free-standing black films of polymers: a model of charged brushes in interaction *Phys. Rev. Lett.* **74** 3628
- [25] Schneck E and Demé B 2015 Structural characterization of soft interfaces by standing-wave fluorescence with x-rays and neutrons *Curr. Opin. Colloid Interface Sci.* **20** 244–52
- [26] Bloch J M et al 1985 Concentration profile of a dissolved polymer near the air-liquid interface: x-ray fluorescence study *Phys. Rev. Lett.* **54** 1039
- [27] Daillant J, Bosio L, Benattar J J and Blot C 1991 Interaction of cations with a fatty acid monolayer. A grazing incidence x-ray fluorescence and reflectivity study *Langmuir* **7** 611–4
- [28] Schneck E et al 2010 Quantitative determination of ion distributions in bacterial lipopolysaccharide membranes by grazing-incidence x-ray fluorescence *Proc. Natl Acad. Sci. USA* **107** 9147–51
- [29] Bedzyk M J, Bilderback D H, Bommarito G M, Caffrey M and Schildkraut J S 1988 X-ray standing waves: a molecular yardstick for biological membranes *Science* **241** 1788–91
- [30] Bedzyk M J, Bommarito G M, Caffrey M and Penner T L 1990 Diffuse-double layer at a membrane-aqueous interface measured with x-ray standing waves *Science* **248** 52–6
- [31] Schneck E et al 2016 Atom-scale depth localization of biologically important chemical elements in molecular layers *Proc. Natl Acad. Sci. USA* **113** 9521–6
- [32] Demé B, Cataye C, Block M A, Maréchal E and Jouhet J 2014 Contribution of galactoglycerolipids to the 3-dimensional architecture of thylakoids *FASEB J.* **28** 3373–83
- [33] Weinbaum S, Tarbell J M and Damiano E R 2007 The structure and function of the endothelial glycocalyx layer *Annu. Rev. Biomed. Eng.* **9** 121–67
- [34] Murat M and Grest G S 1989 Interaction between grafted polymeric brushes: a molecular-dynamics study *Phys. Rev. Lett.* **63** 1074
- [35] Sackmann E 1996 Supported membranes: scientific and practical applications *Science* **271** 43–8

- [36] Wei Z and Prescott S W 2015 Scattering approaches to probing surface layers under confinement *Curr. Opin. Colloid Interface Sci.* **20** 253–60
- [37] Lis L J, McAlister M, Fuller N, Rand R P and Parsegian V A 1982 Interactions between neutral phospholipid bilayer membranes *Biophys. J.* **37** 657
- [38] Petrache H I, Gouliaev N, Tristram-Nagle S, Zhang R, Suter R M and Nagle J F 1998 Interbilayer interactions from high-resolution x-ray scattering *Phys. Rev. E* **57** 7014
- [39] Kenworthy A K, Hristova K, Needham D and McIntosh T J 1995 Range and magnitude of the steric pressure between bilayers containing phospholipids with covalently attached poly (ethylene glycol) *Biophys. J.* **68** 1921
- [40] Cerezo A, Petford-Long A K, Larson D J, Pinitsoontorn S and Singleton E W 2006 The formation mechanism of aluminium oxide tunnel barriers *J. Mater. Sci.* **41** 7843–52
- [41] Vrublevsky I, Parkoun V, Schreckenbach J and Marx G 2003 Effect of the current density on the volume expansion of the deposited thin films of aluminum during porous oxide formation *Appl. Surf. Sci.* **220** 51–9
- [42] Basu J K *et al* 2007 Direct probe of end-segment distribution in tethered polymer chains *Macromolecules* **40** 6333–9
- [43] Leckband D E, Schmitt F J, Israelachvili J N and Knoll W 1994 Direct force measurements of specific and nonspecific protein interactions *Biochemistry* **33** 4611–24
- [44] Wong J Y, Kuhl T L, Israelachvili J N, Mullah N and Zalipsky S 1997 Direct measurement of a tethered ligand-receptor interaction potential *Science* **275** 820–2
- [45] Tamm L and McConnell H M 1984 Supported phospholipid bilayers *Biophys. J.* **47** 105–13
- [46] Azzam R M A and Bashara N M 1987 *Ellipsometry and Polarized Light* (North-Holland: sole distributors for the USA and Canada, Elsevier)
- [47] Adachi S 1988 Model dielectric constants of Si and Ge *Phys. Rev. B* **38** 12966
- [48] Malitson I H 1965 *Interspecimen comparison of the refractive index of fused silica* *JOSA* **55** 1205–9
- [49] Wong J E, Rehfeldt F, Hänni P, Tanaka M and von Klitzing R 2004 Swelling behavior of polyelectrolyte multilayers in saturated water vapor *Macromolecules* **37** 7285–9
- [50] Ruths J, Essler F, Decher G and Riegler H 2000 Polyelectrolytes I: polyanion/polycation multilayers at the air/monolayer/water interface as elements for quantitative polymer adsorption studies and preparation of hetero-superlattices on solid surfaces *Langmuir* **16** 8871–8
- [51] Reiter R, Motschmann H and Knoll W 1993 Ellipsometric characterization of streptavidin binding to biotin-functionalized lipid monolayers at the water/air interface *Langmuir* **9** 2430–5
- [52] Parratt L G 1954 Surface studies of solids by total reflection of x-rays *Phys. Rev.* **95** 359
- [53] Nelson A 2006 Co-refinement of multiple-contrast neutron/x-ray reflectivity data using MOTOFIT *J. Appl. Crystallogr.* **39** 273–6
- [54] Stepanov S and Forrest R 2008 Fitting dynamical x-ray diffraction data over the World Wide Web *J. Appl. Crystallogr.* **41** 958–62